EFFECT OF THE RATE OF MULTIAXIAL COMPRESSION AT ROOM TEMPERATURE ON THE EVOLUTION OF MICROSTRUCTURE OF COMMERCIAL-PURITY ALUMINUM

Y. Yang,[1, 2, 3] **S. J. Yang,**[1] **Z. Wang,**[1] **and X. F. Gao**[1]

Commercial-purity aluminum of grade 1050 obtained by uniaxial or multiaxial compression at room temperature at deformation rates from 1.2×10^3 to 1.0×10^{-3} $\sec^{-1}$ is studied. The true strain per one pass is kept constant while the total strain amounts to 1.6 in uniaxial deformation and to 3.0 in multiaxial one. The microstructure is determined using a transmission electron microscope. The high-rate deformation is shown to be the most effective for refining the structure due to elevation of the dislocation density and suppression of the dynamic recovery.

Key words: strain rate, aluminum, multiaxial compression, grain refinement, dislocation structure.

INTRODUCTION

Most of the methods used to raise the strength of metallic materials commonly lower their ductility and toughness. Simultaneous elevation of strength and ductility may be provided by refinement of grains to a nanosize [1 – 5]. Severe plastic deformation (SPD) draws the attention of specialists as an important method for grain refinement. SPD is conducted by various techniques such as equal channel angular pressing [6 – 10], multiple forging [11, 12], high pressure torsion [13, 14], accumulative roll bonding [15, 16], cyclic extrusion compression [17, 18], etc. The microstructure of the material is refined by changing the deformation trajectory or raising the accumulated strain under SPD. The change of the microstructure during deformation of a low or medium degree is commonly described as division into cell blocks containing conventional dislocation cells. When the strain grows, a lamellar structure appears, the spacing between the boundaries decreases, and the angles of misorientation over the cell boundaries grow [19 – 21]. It has been shown in [11] that the dislocation density may reach saturation with growth in the strain. Therefore, the refinement of grains is restricted and the grain size is commonly about 200 nm. Studies of the evolution of structure in the process of accumulation of strain under SPD have shown that the mechanisms of variation of microstructure differ at high and low deformation rates [22, 23]. The authors of [21] have observed the changes in the structure of pure nickel at deformation rates $10^2 – 10^3$ $\sec^{-1}$. With growth of the strain, the microstructure of the nickel changes from a cellular one to a lamellar one, similarly to its behavior at low deformation rates. However, growth of the deformation rate without changes in the strain causes grain refinement and elevates the dislocation density. After dynamic plastic deformation at cryogenic temperatures, the structure of massive copper acquires a great number of nanosize twins [23, 24]. In contrast to nickel and copper, the stacking fault energy in aluminum is high. Recent works [25, 26] have been devoted to variation of structure in pure aluminum and in aluminum alloy 2195 of the Al – Li system at high deformation rates. However, investigation of the effect of the deformation rate on the microstructure of pure aluminum and its alloys is not yet exhaustive.

The aim of the present work was to study the effect of the deformation rate (within six orders of magnitude) on the microstructure of commercial aluminum 1050 during uniaxial and multiaxial compression at room temperature.

[1] School of Material Science and Engineering, Central South University, Changsha, China.
[2] Institute of Fluid Physics, China Academy of Engineering Physics, Mianyang, China.
[3] Key Laboratory of the Ministry of Education for Nonferrous Metal Materials Science and Engineering, Central South University, Changsha, China.
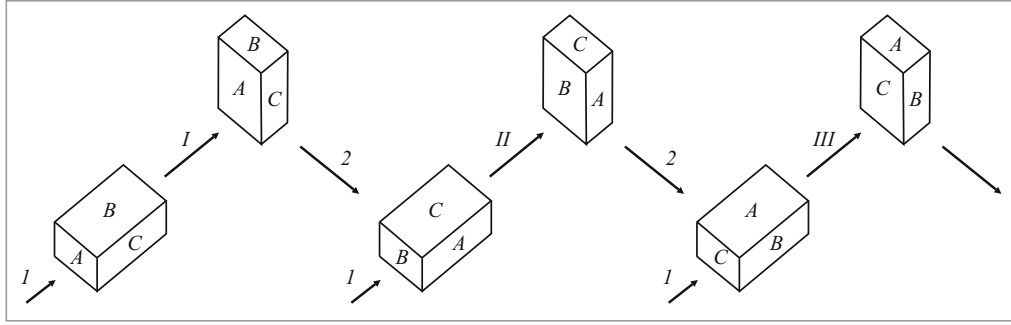
Fig. 1. Scheme of multiaxial compression: *I, II, III*) first, second and third passes; *1*) load; *2*) rotation of specimen.

METHODS OF STUDY

We studied commercial rolled aluminum 1050. Billets with homogeneous coarse grains (46 μm in diameter) were annealed at 673 K for 3 h in a salt-bath furnace. The annealed billets were cut into samples of two types, i.e., cylinders with diameter 22 mm and height 30 mm and rectangular prisms with sizes $12 \times 8 \times 8$ mm. Both types were upset at deformation rates 1.2×10^3 sec^{-1} and 1.0×10^{-3} sec^{-1}. The cylindrical samples were subjected to uniaxial deformation and the rectangular samples were subjected to multiaxial deformation. Figure 1 presents the scheme of multiaxial upsetting. The low-rate deformation was conducted in a universal Instron 3369 testing machine and the high-rate deformation was conducted in an SHPB (Split Hopkinson Pressure Bar) device presented schematically in Fig. 2. In each pass, we determined the strain by formula $\varepsilon = (L_0 / L_f)$, where L_0 and L_f are the initial and final heights of the rectangular prism, respectively. Then we evaluated the total (accumulated) strain. The lubricant used in the upsetting was Vaseline. The strain in each pass of the uniaxial and multiaxial deformation was the same. Both kinds of deformation were implemented in 9 passes. The accumulated strain in the uniaxial upsetting $\varepsilon = 1.6$ after 9 passes; the upsetting in each pass was 15%. The total strain in the multiaxial upsetting $\varepsilon = 3.0$ after 9 passes; the upsetting in each pass was 30%.

The strain pulse signal produced by the SHPB can be used for computing the loading parameters, i.e., the stress σ, the strain ε, and the strain rate ε̇ by the formulas [27]:

$$\varepsilon = -\frac{2C_0}{L_0} \int_0^t \varepsilon_r \mathrm{d}t; \qquad (1)$$

$$\dot{\varepsilon} = \frac{\mathrm{d}\varepsilon}{\mathrm{d}t} = -\frac{2C_0 \varepsilon_r}{L_0}; \qquad (2)$$

$$\sigma = \frac{EA_0}{A} \varepsilon_t, \qquad (3)$$

where C_0 is the speed of propagation of the elastic wave, E is the modulus of elasticity of the impacted sample, L_0 is the height of the not deformed sample, and A_0 and A are cross

sections of the sample before and after the impact, respectively.

The microstructure of the not deformed samples was assessed with the help of polarization microscopy. Metallographic specimens were prepared by electrochemical polishing and anodic oxidation. The polishing electrolyte was composed of 10% $HClO_4$ and 90% H_3CH_2OH. Polishing was conducted at a voltage of 24 V for 45 sec at room temperature. Anodic coatings were obtained in a solution containing 38 ml H_2SO_4, 43 ml H_2PO_4 and 19 ml H_2O) at a voltage of 20 V with a hold for 2 min. Transmission electron microscopy was performed with the help of a Tecnai G220 microscope at an accelerating voltage of 200 kV. The 1.5-mm-thick samples for this study were cut in parallel to the loading direction in uniaxial upsetting near the center of the billet. The samples for multiaxial upsetting were cut from the central part of the billet independently of the loading direction. The 1.5-mm-thick samples were ground to a thickness of 60 – 80 μm and punched into discs with diameter 3 mm. Further thinning was conducted in a double-jet electrochemical device in an electrolyte containing 30% HNO_3 and 70% methanol at a temperature of –25°C and a voltage of 20 V. The grain size was determined from electron microscope images using the Nano Measurer software. The grain boundaries, the cell walls, and the dislocation boundaries with ob-
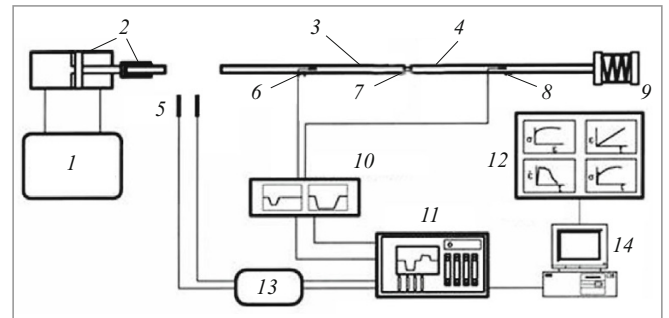
Fig. 2. Scheme of deformation of specimens in the SHPB unit: *1*) pressure control system; *2*) strike bar; *3*) incidental pressure bar; *4*) transmitter pressure bar; *5*) sensor; *6*) strain gage 1; *7*) specimen; *8*) strain gage 2; *9*) dashpot; *10*) signal amplifier; *11*) oscilloscope; *12*) output data; *13*) filter; *14*) computer.
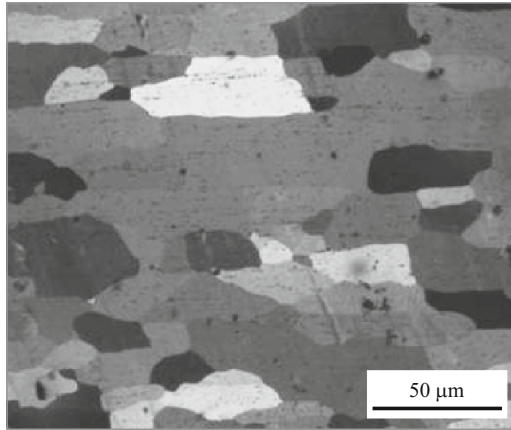
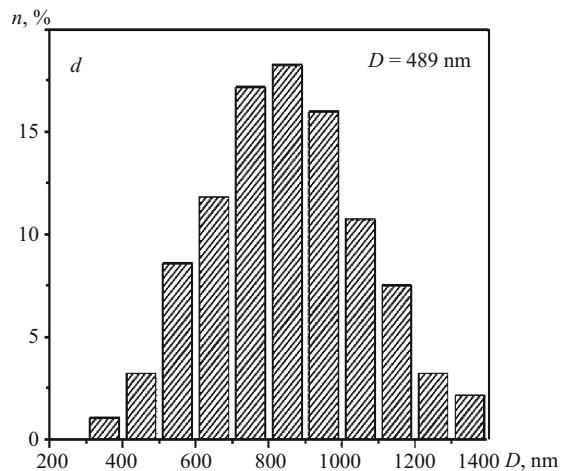**Fig. 3.** Microstructure (optical microscopy) of annealed commercial aluminum 1050.
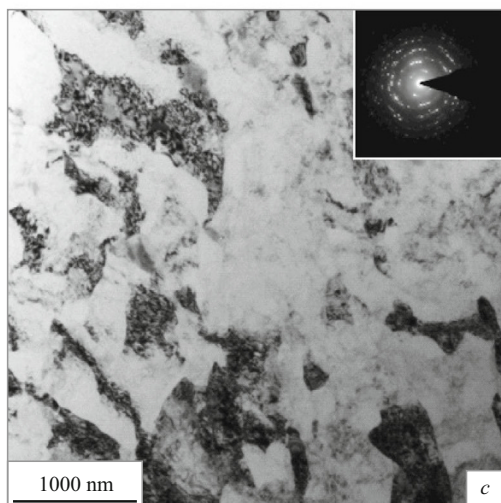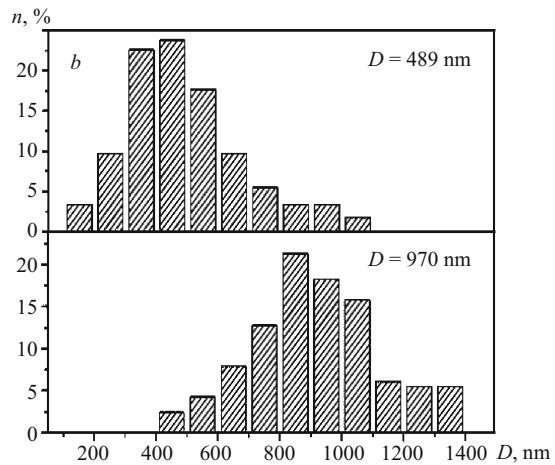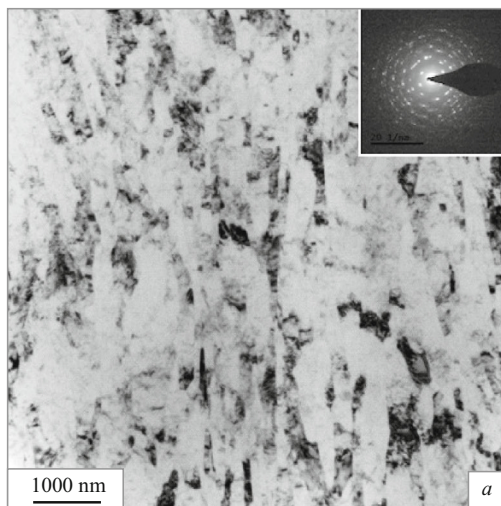
ting the transverse/longitudinal size was understood as the distance between the boundaries perpendicular/parallel to the direction of the elongation, respectively. The average grain size was computed as a result of measurement of 150 grains/cells by the method of random secants (the Heyn lineal intercept method) according to the ASTM Standard E112-96.

RESULTS AND DISCUSSION

Figure 3 presents the microstructure of an annealed sample of commercial aluminum 1050 obtained under an optical microscope. The microstructure is fully recrystallized; the grains are equiaxed and have a mean size of 46 μm.

Figure 4*a* and *b* present the results of transmission electron microscopy of a longitudinal section of a sample after uniaxial upsetting to a strain of 1.6 at a rate of $1 \times 10^{-3} \text{ sec}^{-1}$. We can see a great number of subgrains and dislocation cells elongated perpendicularly to the loading di-

vious contrast were defined as measured boundaries. For the elongated grains/cells in the samples after uniaxial upset-

Fig. 4. Microstructure (transmission electron microscopy) (*a*, *c*) and subgrain/cell size distribution (*b*, *d*) of commercial aluminum 1050 after uniaxial (*a*, *b*) and multiaxial (*c*, *d*) upsetting at a rate of $1 \times 10^{-3} \text{ sec}^{-1}$.
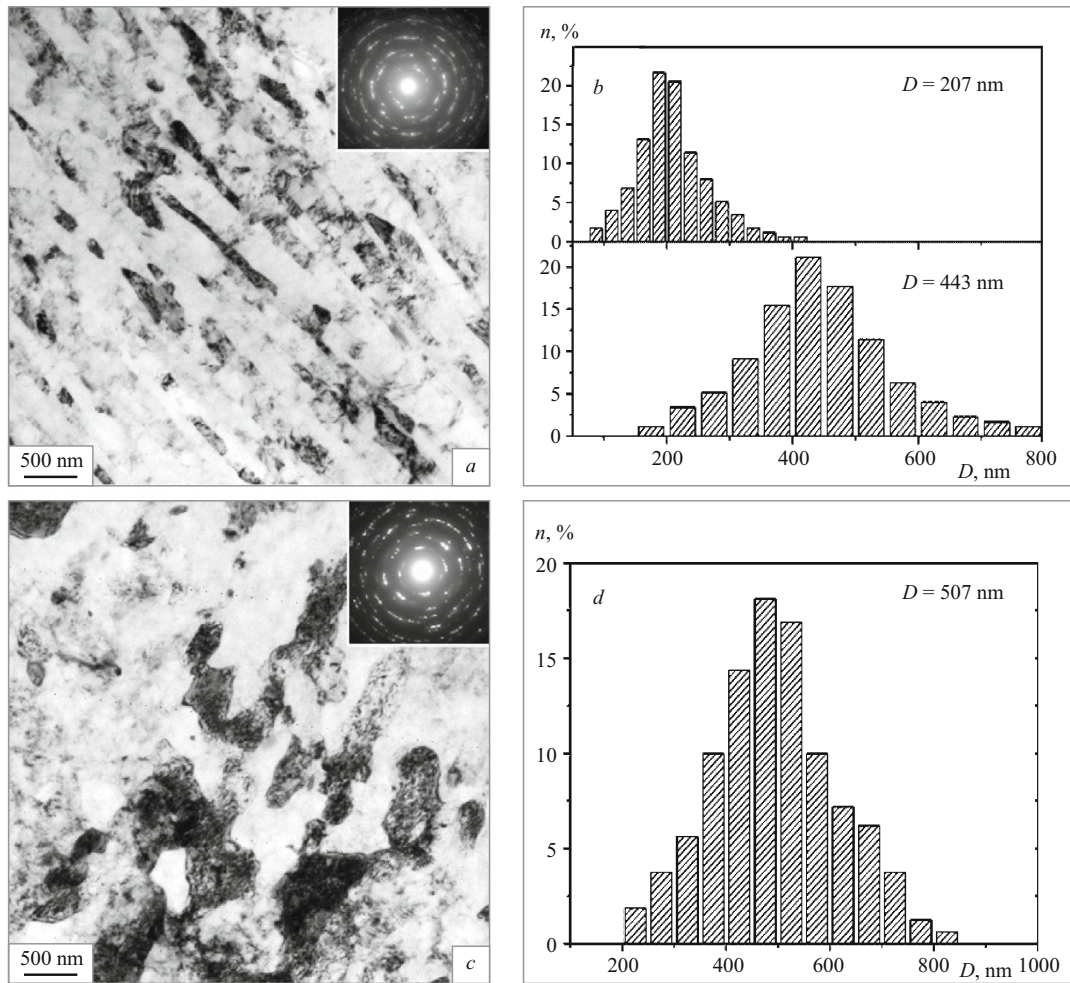
Fig. 5. Microstructure (transmission electron microscopy) (*a, c*) and subgrain/cell size distribution (*b, d*) of commercial aluminum 1050 after uniaxial (*a, b*) and multiaxial (*c, d*) upsetting at a rate of 1.2×10^3 sec^{-1}.

rection. There are elements of a bamboo-like structure containing subgrains and dislocation cells. Many dislocation cells have an extended shape. Some researchers think [20] that these bamboo-like structures form due to growth of strain from blocks (subgrains) containing ordinary dislocation cells. Blocks (subgrains) are typical structural components at low strain. In the lamellar structures we detected dislocation boundaries of two types, i.e., geometrically necessary boundaries (GNB) and auxiliary incident dislocation boundaries (IDB) [28]. The features of such a microstructure resemble those observed after high-strain rolling [29]. The circular diffraction patterns indicate considerable misorientation of the subgrains due to the deformation [20]. At a statistically normal grain size distribution the mean transverse and longitudinal sizes of the structural components are 489 ± 20 and 970 ± 20 nm, respectively (Fig. 4*b*).

Figure 4*c* presents an electron diffraction pattern of a sample after multiaxial upsetting at deformation rate 1×10^{-3} sec^{-1} with strain 3.0. It can be seen that the coarse grains have disappeared giving place to approximately equiaxed dislocation cells and randomly distributed disloca-

tion tangles. The walls of the cells are curved and smeared by dislocations. The ring diffraction patterns reflect considerable misorientation of subgrains and cells. The mean grain/cell size is 874 ± 20 nm. Figure 4*d* presents the normal size distribution of the grains and cells.

The microstructure of the sample in the longitudinal section after uniaxial upsetting at a rate of 1.2×10^3 sec^{-1} with strain 1.6 at room temperature is presented in Fig. 5*a*. The characteristics of the microstructure are similar to those observed under quasi-static uniaxial upsetting. It can be seen that ultrafine elongated grains have formed instead of the initial equiaxed grains. The dominant dislocation configurations are tangles and cells. There are two types of dislocation boundaries, i.e., GNB and IDB. The corresponding rings in the diffraction patterns indicate a high degree of misorientation over these boundaries. The mean size of the structural components in transverse and longitudinal directions is 207 ± 20 and 443 ± 20 nm, respectively. This is less than in the sample after quasi-static uniaxial upsetting. As in the previous case, the size distribution is a normal one (Fig. 5*b*).

The microstructure of the sample after multiaxial upsetting at a rate of 1.2×10^3 sec^{-1} with strain 3.0 is presented in Fig. 5c. It can be seen that the density of tangles in the dislocation cells is higher than in the case of quasi-static multiaxial deformation (Fig. 5c). Like in the microstructure obtained due to deformation at a rate of 1×10^5 sec^{-1} [26], the high dislocation density results in widening of the walls of the dislocation cells and smearing of the boundaries. We can also observe ultrafine equiaxed subgrains. The contrast between some neighbor subgrains is high, which indicates their misorientation, and the diffraction patterns exhibit rings. The mean subgrain/cell size is 507 ± 20 nm, which is much smaller than after the quasi-static multiaxial upsetting (1.0×10^{-3} sec^{-1}). Figure 5d presents the normal size distribution of the components.

Several mechanisms have been suggested for describing the multiplication of dislocations in the case of high-rate deformation [27, 30, 31]. It is presumed that a shock stress wave propagates over the loading direction. As a rule, the dislocation density under high-rate loading is $10^3 - 10^4$ times higher than the dislocation density under static loading. According to Orowan, the dislocation density is proportional to the shear rate [32], and he size of the subgrains/dislocation cells D_c is related to the total dislocation density ρ as [33]

$$D_c \approx K \rho^{-1/2}, \qquad (4)$$

where K is a constant. Accordingly, we observe refinement of the structure at a high deformation rate.

CONCLUSIONS

1. Uniaxial upsetting of coarse-grained commercial aluminum 1050 results in formation of subgrains and dislocation cells with a bamboo-like structure in the place of coarse grains. The main dislocation configurations are tangles and cells. Increase in the deformation rate by six orders of magnitude (to 1.2×10^3 sec^{-1}) results in refinement of the components by about a factor of 2. The transverse and longitudinal sizes of the bamboo-like structure after the high-rate deformation are 200 and 440 nm, respectively.

2. After multiaxial upsetting, the subgrains/dislocation cells are approximately equiaxed. The size of the subgrains/cells after the high-rate deformation is 500 nm, and that after the slow-rate deformation is 870 nm.

3. Increase in the deformation rate of commercial aluminum 1050 refines the structure more effectively than increase in the degree of the deformation.

REFERENCES

1. M. A. Meyers, A. Mishra, and D. J. Benson, *Progr. Mater. Sci.*, **51**, 427 – 556 (2006).
2. K. S. Kumar, H. V. Swygenhoven, and S. Suresh, *Acta Mater.*, **51**, 5743 – 577 (2003).
3. Y. M. Yang, K. Wang, and D. Pan, *Scr. Mater.*, **48**, 1581 – 1586 (2003).
4. V. M. Imayev and G. A. Salishchev, *Scr. Mater.*, **40**, 183 – 190 (1998).
5. Z. Horita, T. Fujinami, and M. Nemoto, *J. Mater. Proc. Technol.*, **117**, 288 – 292 (2001).
6. V. M. Segal, V. I. Reznikov, A. E. Drobyshevskiy, and V. I. Kopylov, *Russian Metallurgy*, **1**, 99 – 105 (1981).
7. V. M. Segal, *Mater. Sci. Eng. A*, **338**, 331 – 344 (2002).
8. R. Z. Valiev, Y. Estrin, Z. Horita, et al., *JOM*, **58**, 33 – 39 (2006).
9. V. M. Segal, *Mater. Sci. Eng. A*, **197**, 157 – 164 (1995).
10. R. Z. Valiev and T. G. Langdon, *Progr. Mater. Sci.*, **51**, 881 – 981 (2006).
11. Y. Z. Wu and H. G. Yan, *Mater. Sci. Eng. A.*, **556**, 164 – 169 (2012).
12. A. Belyakov, T. Sakai, H. Miura, and K. Tsuzaki, *Philos. Mag. A*, **81**, 2629 – 2643 (2001).
13. A. Azushima, R. Kopp, A. Korhonen, et al., *CIRP Annals Manuf. Technol.*, **57**, 716 – 735 (2008).
14. A. Vorhauer and R. Pippan, *Scr. Mater.*, **51**, 921 – 925 (2004).
15. Y. Saito, H. Utsunomiya, N. Tsuji, and T. Sakai, *Acta Mater.*, **47**, 579 – 583 (1999).
16. N. Tsuji, Y. Saito, S. Lee, and Y. Minamino, *Adv. Eng. Mater.*, **5**, 338 – 344 (2003).
17. J. Richert and M. Richert, *Aluinum*, **62**, 604 – 607 (1986).
18. M. Richet, H. P. Stuwe, M. J. Zehetbauer, et al., *Mater. Sci. Eng. A*, **355**, 180 – 185 (2003).
19. H. W. Zhang, X. Huang, and N. Hansen, *Acta Mater.*, **56**, 5451 – 5465 (2008).
20. D. A. Hughes and N. Hansen, *Acta Mater.*, **45**, 3871 – 3886 (1997).
21. Z. P. Luo, H. W. Zhang, N. Hansen, and K. Lu, *Acta Mater.*, **60**, 1322 – 1333 (2012).
22. H. J. Mc Queen and J. F. Hockett, *Metall. Trans.*, **1**, 2997 – 3004 (1970).
23. Y. S. Li, N. R. Tao, and K. Lu, *Acta Mater.*, **56**, 230 – 241 (2008).
24. F. Yan, H. W. Zhang, N. R. Tao, and K. Lu, *J. Mater. Sci. Technol.*, **27**, 673 – 679 (2011).
25. Yang Yang, Fei Ma, Hai Bo Hu, et al., *J. Mater. Res.*, **606**, 3502 – 3509 (2014).
26. Yang Yang, Ya Dong Chen, Hai Bo Hu, et al., *J. Mater. Res.*, **30**, 3502 – 3509 (2016).
27. M. A. Meyers, *Dynamic Behavior of Materials*, John Wiley & Sons Inc., New York (1994), pp. 1557 – 1562.
28. D. Kuhlmann-wildorf and N. Hansen, *Scr. Metall. Mater.*, **25**, 1557 – 1562 (1991).
29. Z. Y. Yao, Q. Liu, and A. Godfrey, *Acta Metall. Sinica*, **45**, 647 – 651 (2009).
30. M. A. Mogilevsky, *Mechanisms of Deformation under Shock Loading*, Springer US (1981), pp. 531 – 546.
31. M. A. Meyers, *Scr. Metall.*, **12**, 21 – 26 (1978).
32. R. W. Cahn and P. Hansen, *Physical Metallurgy*, The Netherlands, North-Holland, Amsterdam (1996), Vol. 4, pp. 1869 – 1870.
33. D. L. Holt, *J. Appl. Phys.*, **41**, 3197 – 3201 (1970).